ADVANCED FUNCTIONAL MATERIALS
www.afm-journal.de

Chiral SURMOFs for Vibrational Circular Dichroism: Multiscale Modeling and Experimental Insights

Ana C. Fingolo, Nadine von Coelln, Benedikt Zerulla, Marjan Krstić, Christian Huck, Thomas G. Mayerhöfer, Christoph Krafft, Petra Tegeder, Carsten Rockstuhl,* and Christof Wöll**

Chiral surface-anchored metal-organic frameworks (SURMOFs) are emerging as versatile platforms for enantioselective separation, sensing, and the manipulation of circularly polarized light. To harness their full potential, predictive modeling of their optical properties is essential, given the vast design space. Here, a multiscale computational framework is introduced that reliably captures the optical response of camphoric acid–DABCO-based pillar-layer SURMOFs incorporating either zinc or copper nodes. The approach integrates simulations from the unit-cell level to the thin-film scale. To validate the model, SURMOFs are fabricated on various substrates and characterized using infrared reflection and transmission spectroscopy, infrared scanning near-field optical microscopy, and solid-state vibrational circular dichroism (VCD) spectroscopy. Notably, the VCD spectra for the zinc-based SURMOF provide direct insight into vibrational optical activity in the solid state. The strong correlation between theoretical predictions and experimental data confirms the robustness of the model and establishes design principles for future optically active chiral MOF materials.

1. Introduction

Over the past three decades, metal-organic frameworks (MOFs) have been extensively investigated and applied in various fields.[1,2] Characterized by their crystalline structures and remarkable porosity, they are formed by the coordination of multidentate organic ligands with metal ions or clusters, which are referred to as secondary building units (SBUs). Since the pioneering studies of Yaghi et al.[3] and Kitagawa et al.,[4] significant interest has been generated in this class of materials. To date, thousands of MOF structures have been predicted and synthesized.[5] Due to their high porosity, large surface area, and structural tunability, MOFs have been effectively used in many applications, such as gas storage,[6] gas separation,[7,8] catalysis,[9,10] biomedical applications,[11] and sensing.[12,13]

Because most MOFs are obtained as powders, their direct integration into solid-state devices is often challenging.[14] To overcome this limitation, surface-anchored metal-organic frameworks (SURMOFs) were developed.[15] These thin MOF films are grown on functionalized substrates via layer-by-layer liquid-phase epitaxy, ensuring strong adhesion, controllable thickness, and often well-defined crystalline orientation.[16] This layer-by-layer approach makes SURMOFs especially attractive as platform materials for optical studies, since in powder MOFs, scattering and self-attenuation effects severely complicate measurements of photophysical parameters, and a characterization using AFM-related techniques is almost impossible.[17,18] The growth of SURMOFs has been investigated in a wide range of substrates and synthesis conditions providing a good basis for the synthesis conditions used in this work.[19,20]

A particularly interesting subgroup are chiral SURMOFs, which incorporate chiral linkers in their structures. Their ability to interact differently with left- and right-handed circularly polarized light opens opportunities for enantioselective separation,[21] sensing,[2] and optoelectronic applications such as the emission or detection of circularly polarized light.[22] Importantly, this property also allows for the use of a somewhat underexplored spectroscopic tool for MOFs: vibrational circular dichroism (VCD). VCD is usually performed in solution and probes vibrational transitions in the electronic ground state. However, solid-state VCD can provide sharper spectral features

A. C. Fingolo, C. Wöll
Institute of Functional Interfaces
Karlsruhe Institute of Technology (KIT)
76131 Karlsruhe, Germany
E-mail: christof.woell@kit.edu

N. von Coelln, C. Huck, P. Tegeder
Physikalisch-Chemisches Institut
Universität Heidelberg
Im Neuenheimer Feld 253, 69120 Heidelberg, Germany
E-mail: tegeder@uni-heidelberg.de

B. Zerulla, C. Rockstuhl
Institute of Nanotechnology
Karlsruhe Institute of Technology (KIT)
Kaiserstr. 12, 76131 Karlsruhe, Germany
E-mail: carsten.rockstuhl@kit.edu

M. Krstić, C. Rockstuhl
Institute of Theoretical Solid State Physics
Karlsruhe Institute of Technology (KIT)
Kaiserstr. 12, 76131 Karlsruhe, Germany

T. G. Mayerhöfer, C. Krafft
Leibniz Institute of Photonic Technology
Albert-Einstein-Str. 9, 07745 Jena, Germany

DOI: 10.1002/adfm.202524088

and stronger signals due to the reduced conformational flexibility.[23,24] For conventional powdered MOFs, solid-state VCD requires embedding in KBr pellets, which can reduce the signal-to-noise ratio.[25,26] In contrast, SURMOFs can be grown directly on transparent rigid substrates (e.g., CaF_2), eliminating the need for such preparation and making them ideally suited for solid-state VCD.[27] In addition, since SURMOFs can be grown with well-defined crystalline orientations, they also allow for orientation-dependent VCD measurements, providing additional insight into anisotropic vibrational responses.

Given the vast design space of possible SURMOFs, predictive modeling is crucial to guide experimental exploration, narrowing the sample space for experimental screening.[28] However, before a theoretical model can be widely adopted, its predictions must be validated through comparison with experimental data. Recently, a number of studies[29–31] utilized an approach combining scattering theory based on Jones matrix calculus[32] for fully polarized light to design and manufacture complex metasurfaces by controlling the chiral response of individual metaatoms. Those applications were directed towards the independent phase manipulations, creation of vortex beams with further potential applications in optical imaging. In contrast, our approach combines atomistic quantum chemistry simulations with more general T-matrix scattering theory[33] to address material properties in the infrared part of the electromagnetic spectrum. Here, we present a multiscale modeling approach that operates across multiple length scales, starting with simulations of a single MOF unit cell and extending to the modeling of thin films of the material.[34] The multiscale modeling workflow combines precise quantum chemistry calculations of circular response of hybrid metal-organic molecules at the atomistic scale[35–38] with electromagnetic scattering simulations[39,40] of larger objects with tailored chiral response.[41,42] We show that our model can provide a broad range of optically observable quantities, such as infrared reflection and transmission, infrared scanning near-field optical microscopy (IR-SNOM), electronic circular dichroism (ECD), as well as VCD, with very good agreement with the experimental results. By aligning theory and experiment, this study demonstrates that SURMOFs are a promising platform for solid-state VCD, while also showing the predictive power of our multiscale model for guiding future material design.

2. Results and Discussion

2.1. Synthesis of the Chiral SURMOFs

The two SURMOFs investigated in this study were composed of either Cu(II) or Zn(II) as the metal centers (**Figure 1a**). Copper is one of the most commonly used metals in SURMOF synthesis, while zinc has environmental advantages and requires less computational power for the simulations. Because of the quenching of electronic excitations by Cu^{2+} dimers, Zn-based SURMOFs are more suitable for detailed photophysical studies and for validation of the simulation method.[43] Camphoric acid and diazabicyclooctane (DABCO) were used as organic linkers to obtain pillar-layer SURMOFs (Figure 1b). These SURMOFs usually are designated as $[Cu_2(Xcam)_2(dabco)]$ or $[Zn_2(Xcam)_2(dabco)]$, but for ease of reading, they will be referred to as Cu-XMOF and Zn-XMOF in this work, where **X** represents the **D** or **L** enantiomer of camphoric acid, respectively. Both SURMOFs feature a similar pillar-layer structure (tetragonal space group, $P42_12$), in which the two distinct organic linkers interact differently with the SBU. The carboxyl groups in camphoric acid, containing two oxygen donor atoms, preferentially coordinate to the equatorial sites of the SBU,[44] forming 2D layers. In contrast, nitrogen-containing molecules such as DABCO preferably coordinate axially to the metal paddlewheel, acting as pillars connecting the 2D layers (Figure 1c).

The selection of camphoric acid as a linker was motivated by its two chiral centers that can exhibit the configurations 1R,3S (D-Cam) or 1S,3R (L-Cam). This intrinsic chirality is particularly relevant for applications such as enantiomer separation, chiral recognition, and asymmetric catalysis.[46–48] Moreover, the chiral nature of camphoric acid imparts the ECD activity to the resulting SURMOF.[49] ECD spectroscopy is a well-established technique for characterizing chiral compounds, including chiral MOFs.[50–52] The extension of regular CD into the infrared region is called VCD, and it can be especially interesting due to the larger number of vibrational states compared to electronic states.[53] In this way, VCD can help further characterize the SURMOF structure, and we explore this technique with both simulation and experimental attempts.

During SURMOF growth, some differences in nucleation and adhesion to the substrate of these SURMOFs were observed under the same set of conditions, with the Cu-MOF performing better. Therefore, as a standard, first some layers of Cu-MOF were grown on the substrates to act as a seeding layer for the subsequent deposition of Zn-MOF.[54]

The Cu-MOF and Zn-MOF crystallites form platelet structures, as can be seen in the atomic force microscopy (AFM) image in Figure S3 (Supporting Information), which can be oriented in the (100) direction with DABCO pillars perpendicular to the substrate, or in the (001) direction, where the pillar linker lies parallel to the substrate. The presence of both, platelets lying flat on the substrate as well as ones standing upright, indicates that a perfect orientation could not be achieved under our synthesis conditions. The presence of mixed orientation crystals is confirmed by the X-ray diffraction (XRD) diffractograms shown in Figure 1d, where the data obtained in this work is compared to the powder diffraction pattern of Zn-MOF reported in the literature.[45] In the out-of-plane measurement, both the (001) and (200) reflections are observed, indicating that crystallites with different orientations coexist within the film. However, the relatively low intensity of the (200) peak compared to the powder diffraction suggests that the (001) orientation is predominant in the films. Due to their close diffraction angles, the (001) and (110) peaks could not be distinguished with the resolution available in this setup. Diffractograms corresponding to other substrate types are provided in the Supporting Information.

2.2. Theoretical Characterization

In this subsection, we describe the optical characterization of the SURMOFs using a computational approach. Simulations were carried out using a multi-scale approach that connects

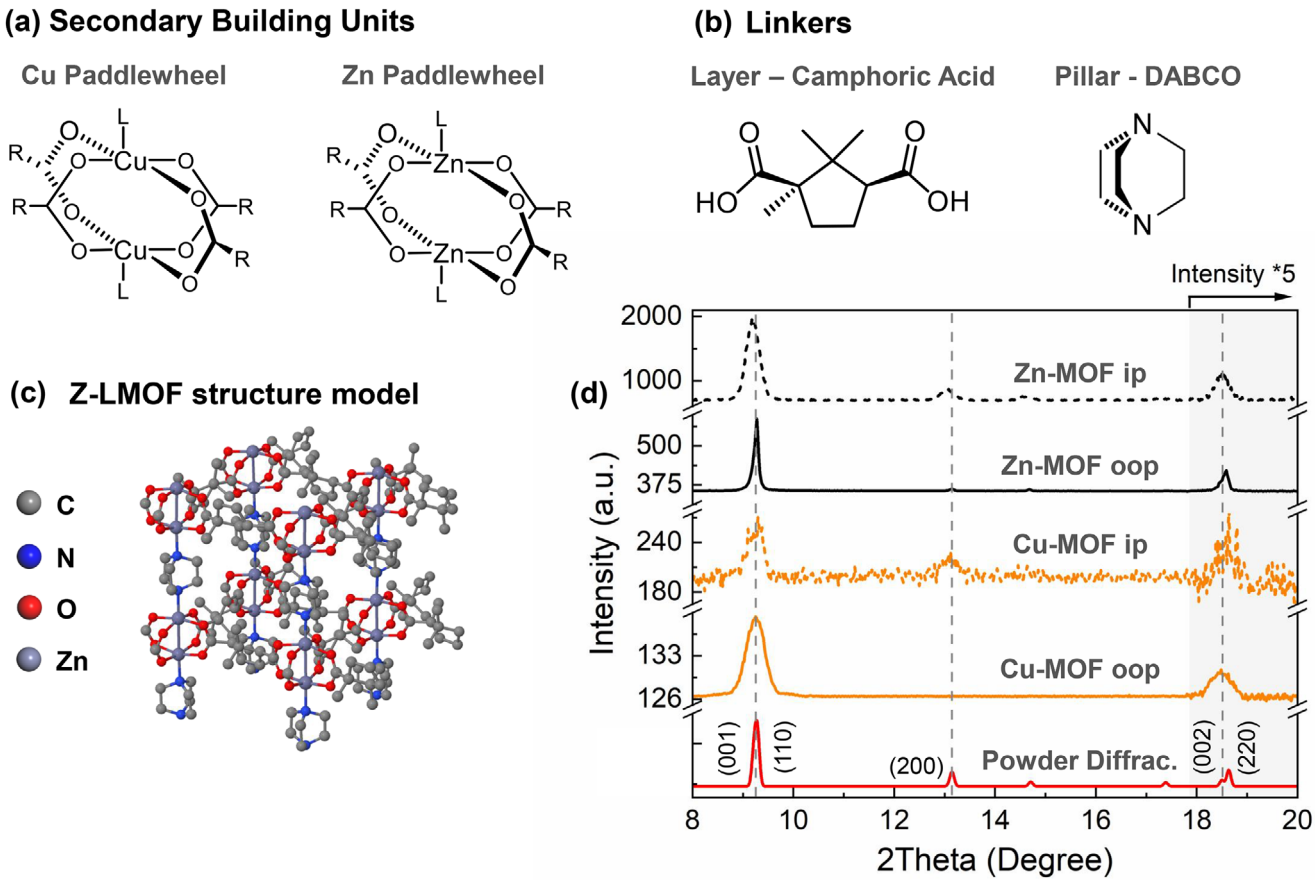

Figure 1. SURMOF a) SBU and b) linkers, c) Z-LMOF unit cell, d) comparison of Zn-MOF powder diffractogram reported in literature[45] with in- and out-of-plane diffractograms of both SURMOFs grown on CaF_2 (from 17.6° the intensity was multiplied by five for a better visualization of the peaks).

quantum-chemistry calculations to Maxwell scattering simulations. Hence, it covers several length scales, from a single molecular periodic unit cell to the thin-film level.[34,55]

2.2.1. Molecular Models and Quantum Chemistry Calculations

The simulation process started by defining and optimizing the molecular models of left (L) and right (D) enantiomers of both Cu- and Zn-MOFs. The unit cell of each MOF was built with the metal-paddle wheel units connected in the x- and y-directions to the chiral camphoric acid molecules and along the z-direction to the pillar linker, DABCO. Such structures are bianisotropic. Unit cell vectors and molecular structure within the unit cell of each MOF type were fully optimized using periodic density functional theory (DFT) software CP2K.[56] Details of the optimization procedure are provided in the Supporting Information. Upon obtaining optimized unit cells, finite-size molecular models were constructed by stacking two unit cells of each MOF in the x-, y-, and z-direction, respectively. Finally, broken covalent bonds at the boundaries of the periodic cells were saturated by additional hydrogen atoms to stabilize the wave function of the finite-size molecular models. The fully optimized enantiomer Zn-LMOF finite-size model, composed of 640 atoms in total, is depicted in Figure 1c (H atoms were omitted for clarity). The other enantiomer models can be found in the Supporting Information. The optimization shows that Cu-MOF has ≈2% smaller volume of the periodic supercell compared to Zn-MOF.

With finite-size molecular models at hand, the calculation of the optical properties of these MOF materials was carried out in the ultraviolet–visible (UV–vis) and infrared (IR) parts of the electromagnetic spectrum using the TURBOMOLE electronic structure program.[57,58] This wave-function-based approach allowed us to obtain accurate damped complex dynamic polarizability tensors for both vibrational and electronic excitations.

Three theoretical approaches have been used for the simulation models for Zn-MOF: one full 3D periodic calculation of the SURMOF bulk material based on a numerical differentiation approach in CP2K (Figure S8, Supporting Information) and two finite-size molecular model calculations using TURBOMOLE, shown in **Figure 2** (top) with focus on the spectral window from 1100–1750 cm^{-1}. The first finite-size model had fixed additional hydrogen atoms added to stabilize the electronic structure of broken covalent bonds on the boundaries of the supercell. In contrast, the second finite-size model had the same hydrogen atoms having extremely large atomic mass, but allowed them to form vibrational modes of the molecular structure. The periodic DFT calculation captures both experimentally observed peaks at 1625 and 1470 cm^{-1}, with the theoretical results slightly red-shifted by 10 cm^{-1} with respect to the experimental data, Figure S8

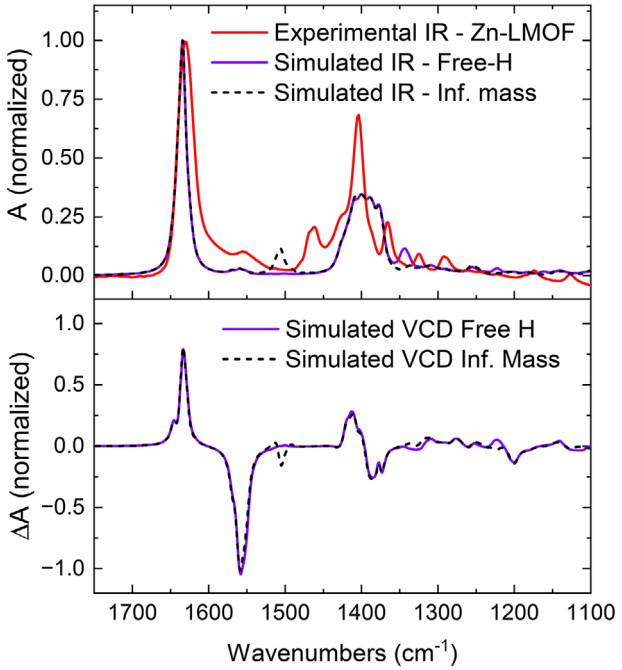

Figure 2. Comparison of simulated and experimental IR (top) and simulated VCD spectra (bottom) based on the finite-size molecular models.

(Supporting Information). It is worth stating that for Cu-MOF a very similar IR absorption spectra compared to the one presented here for Zn-MOF have been reported previously.[22,59] Both finite-size models correctly capture the IR absorption peak at 1625 cm^{-1}, but behave differently in the lower part of the spectral window. Only the model with free "infinite" mass hydrogen atoms indicates the presence of absorption in the range 1500–1550 cm^{-1}, Figure 2. Thus, that molecular model was utilized in all subsequent calculations of the dynamic polarizabilities necessary for the transition to the Maxwell description of the light–matter interactions. Finally, simulated VCD spectra of Zn-LMOF are presented and compared with the experimental result. Both spectra obtained with two different finite-size molecular models show the same spectral features in the wavenumber window of interest. The full vibrational IR absorption and VCD spectra of Zn-LMOF are given in Figure S9 (Supporting Information).

Additional comparison of the electronic circular dichroism is presented in Figure S10 (Supporting Information) to confirm that the theoretically obtained structures correspond to the prepared SURMOF materials used in the experimental study. The figure demonstrates that the quantum chemistry simulations of the atomistic SURMOF models reproduce all observed spectral features. Both peaks at 220 and 180 nm are resolved in the simulations, thus giving confidence that the same material is being considered.

In a last step, the obtained dynamic electric-electric, electric-magnetic, and magnetic-magnetic polarizability tensors were used to construct transition matrices (T-matrices) as used in Maxwell scattering simulations of deposited SURMOF thin films.

2.2.2. Maxwell Scattering Simulations

This paragraph discusses the effective material parameters and the optical response of the Zn-DMOF, obtained with Maxwell scattering simulations. The simulations are based on the T-matrix formalism and are described in the Supporting Information. First, the SURMOF's effective permittivity and chirality obtained with the T-matrix-based homogenization procedure from ref. [60] were analyzed. In this context, two different sets of material parameters are considered. For the first set, the orientation and lattice constants of the SURMOF unit cell were considered as shown in Figure 1c. In this case, the effective material parameters are anisotropic. For the second set, the T-matrix of the unit cell over all possible orientations was averaged, along with the lattice constants. In this case, the effective material parameters are isotropic. The reason why two different sets of material parameters were considered lies in the distinct nature of the measurement techniques used in this article to experimentally obtain the optical properties of the SURMOF samples. As can be seen in Figure 1d, the SURMOF consists of different crystallites showing different orientations with respect to each other. Optical far-field measurements, therefore, exhibit the response averaged over different crystalline orientations. For this case, the isotropic effective material parameters obtained from the averaged T-matrix were analyzed. Importantly, the way in which optical properties are averaged depends on the size of the crystallites relative to the wavelength of light. If the domains are optically small - that is, significantly smaller than about one-tenth of the wavelength - the sample can be treated as effectively homogeneous, and averaging over the dielectric functions (or refractive indices), as obtained from the averaged T-matrix, is appropriate. In contrast, if the domains are optically large, the spectral response - i.e., reflectance or transmittance - must be averaged, as birefringence occurs within each crystallite. This distinction is critical, as it influences band shapes, peak positions, and relative intensities in dependence of the oscillator strengths.[61] Since the crystallite sizes in the samples under consideration are generally much smaller than the wavelength, the first averaging approach is applicable. However, optical near-field measurements, such as SNOM characterization methods, potentially reveal the dependence of the optical response on the orientation of the crystallite of the SURMOF being investigated. In this case, the anisotropic effective material parameters are analyzed.

Figure 3a, b depict the diagonal entries of the anisotropic effective permittivity and chirality. It can be observed that the xx– and yy–components are almost the same for the permittivity. The zz–component is considerably different for both permittivity and chirality and shows a significant resonance at 1600 cm^{-1}, which is related to a DABCO linker resonance.

To compare the calculated permittivity with experimental data, **Figure 4**a, b depict the respective isotropic quantities, and the permittivity obtained from measurements. To model the experimental permittivity measured in infrared reflection absorption spectroscopy (IRRAS) geometry, we used the commercial software package SCOUT.[62] SCOUT applies the transfer-matrix method to calculate optical spectra such as reflection or transmission of layered systems, taking into account

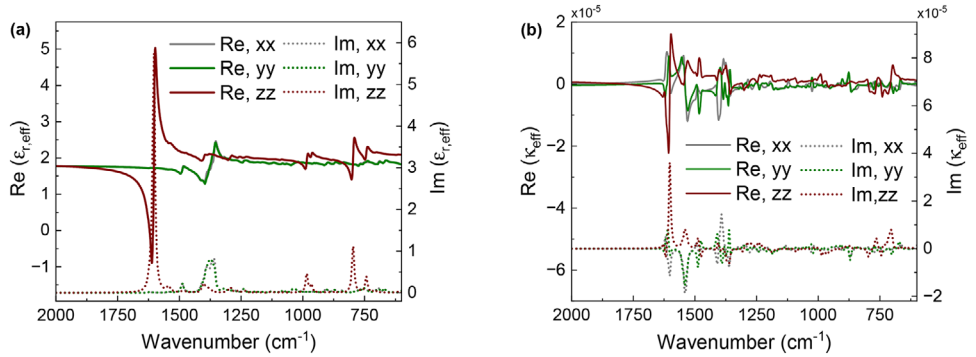

Figure 3. Diagonal entries of the a) effective permittivity and the b) effective chirality tensor for the fixed orientation of the SURMOF unit cell displayed in Figure 1c.

multiple reflections at the interfaces. For each material within the layer stack, the optical properties are described by a model of its dielectric function. The optical model includes the definition of the layer sequence, layer thicknesses, and the dielectric function of each material involved. The dielectric function of the SURMOF material was modeled by a high-frequency dielectric constant ϵ_∞ and 32 Brendel oscillators, which account for the IR-active vibrational modes. The oscillator parameters, namely central position, strength, and Gaussian broadening, were treated as fit parameters, while the Lorentzian damping was fixed at 2 cm^{-1}. Since ϵ_∞ cannot be reliably determined from IRRAS measurements alone, and would require additional spectroscopic ellipsometry data, we adopted a fixed value of $\epsilon_\infty = 2.0$ based on results from optical simulations. The fitting routine employed the downhill simplex algorithm to minimize the mean squared deviation between the simulated and experimental spectra. In this experimentally retrieved permittivity, the resonance at 1600 cm^{-1} is much less prominent than in the simulation of the isotropic effective permittivity. From this observation, it was deduced that for reflection measurements, the xx- and yy-components of the SURMOF material parameters are dominant which is in good agreement with the morphology of the film shown in Figure S3a (Supporting Information) where mostly upstanding platelets are observed.

2.3. Experimental Characterization

2.3.1. Comparison Between Thin-Film Simulations and Experimental Results

In the next step, the different quantities that express the optical response obtained in experimental measurements were compared to predictions from the multi-scale simulations. For this purpose, the SURMOF unit cell, averaged over all possible orientations, was used in the simulations. The squared power reflectance R^2 (calculated because in the reflection measurements the light passes the sample twice), the power transmittance T, and the vibrational circular dichroism spectra ΔA are shown in **Figure 5**. Note that to quantify the circular dichroism, what is commonly known as the differential absorbance was considered. It is here defined as

$$\Delta A = A_+ - A_- \tag{1}$$

where

$$A_\pm = -\log_{10}(T_\pm) \tag{2}$$

is the absorbance of left- (+) and right-handed circularly (−) polarized light, respectively. $T_\pm$ is the respective power transmittance. We stress that to determine the physically correct absorbance, knowledge of reflectance is also required. However, while keeping that definition consistent between experiment and simulation, the quantity as defined above contains all the relevant information.

The values of ΔA simulated for Zn-LMOF were multiplied by −1 to obtain the simulated Zn-DMOF spectrum. The thickness of the films used for the VCD measurement is estimated at around 900 nm (Figure S4, Supporting Information). The films of each enantiomer consist of 20 % Cu-MOF and 80 % Zn-MOF. However, in the simulations, it was assumed that the films consist of 100 % Zn-MOF. The films were deposited on a CaF_2 substrate and subsequently illuminated from the air side with left- and right-handed circularly polarized light.

For the power reflectance and transmittance spectra, shown in Figure 5a,b, a good agreement was observed between the experimentally measured and simulated values in the spectral range from 1800 to 900 cm^{-1}, but quantitative deviations are seen for relative intensities and band positions. Again, simulated absorption is overestimated at 1625 cm^{-1}, like in Figure 4a, compared to experiments. However, it is difficult to pinpoint the exact origin of that misalignment. This could be related to the presence of Cu-MOF. However, this material exhibits a very similar geometric structure to the Zn-MOF, with the only difference per unit cell being the two metal atoms, neighbors in the periodic table of elements. Thus, both materials are expected to have very similar optical responses, especially in the IR part of the electromagnetic spectrum. Using a more complex model with 20% Cu-MOF topped by 80% Zn-MOF in our multiscale workflow would not significantly change the overall optical response. On the other hand, a reduced experimental signal might stem from imperfections in the prepared material, such as disorder

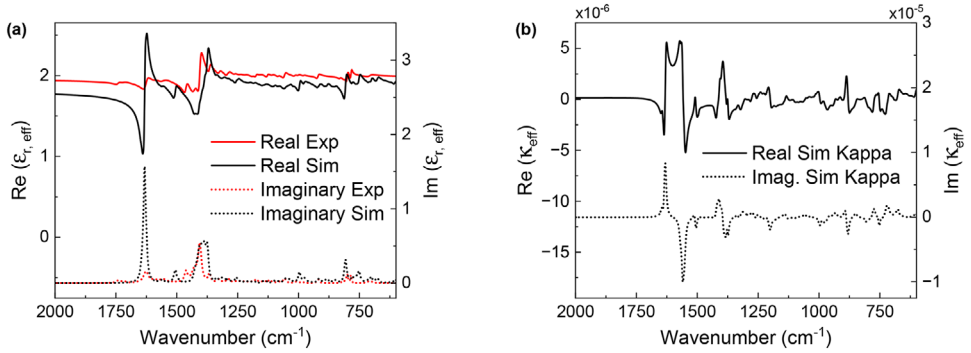

Figure 4. a) Experimentally retrieved and simulated isotropic effective permittivity. b) Simulated isotropic effective chirality. The simulated isotropic material parameters have been obtained for the SURMOF unit cell averaged over different orientations.

in the Cu-MOF seed layers or defects in the film. Unfortunately, such possibilities are unavoidable and difficult to control.

The vibrational circular dichroism spectra (Figure 5c,d) show even better agreement since, in this case, both the positions of the peaks and the relative intensities match the simulation. The experimental VCD spectra exhibit a small systematic offset (negative for Zn-LMOF and positive for Zn-DMOF). Such offsets are commonly encountered in solid-state VCD and may originate from imperfect baseline correction, residual birefringence of the substrate, or minor polarization leakage in the setup. Importantly, the relative features - i. e., the positions and signs of the VCD bands at 1636, 1556, 1417 and 1404 cm^{-1} - are unaffected, and the expected mirror-symmetry between enantiomers is clearly observed. We therefore attribute the offsets to experimental artifacts and note that they do not influence the validity of the comparison between simulation and experiment. Except for the small band near 1500 cm^{-1}, the simulated and experimental VCD spectra coincide really well.

The two resonances around 1600 cm^{-1} are more prominent in the VCD measurements. This indicates that the zz-component of the chirality tensor, shown in Figure 3b, is not smoothed out. This could be due to a larger number of crystallites with unit cells whose z-axis is in the plane of illumination, in comparison to reflectance and transmittance measurements. Additionally, the presence of the Cu-MOF has been neglected in the simulations. Importantly, it was possible to perform the solid-state VCD measurements directly on the SURMOFs grown on transparent substrates, without the need for additional sample preparation such as embedding in KBr pellets. This direct measurement approach represents a significant advantage, as it improves the signal-to-noise ratio and preserves the integrity of the films.

The results presented here have confirmed the capability of the model to define which vibrational modes of the SURMOF are more active in which spectroscopy technique. One distinct difference between the techniques is the peak around 1558 cm^{-1}, which is one of the most intense for VCD but not nearly as strong in IR, and the model was able to predict this difference that could be surprising with experiments alone. In general, the agreement between the experimentally measured and simulated spectra is very good.

2.3.2. Experimental Demonstration of Anisotropic Infrared Properties

The far-field infrared microscopy spectra in reflection and transmission geometry (shown in Figure 5a, b) display an averaged response over different crystal orientations, as conventional far-field infrared microscopy is a diffraction-limited technique, which constrains the spatial resolution in the mid-infrared to multiple micrometers. Thus, it is not possible to record the spectral response of individual crystals. To overcome this limitation of spatial resolution and investigate the anisotropic infrared properties of the material, IR-SNOM was utilized. The technique combines an AFM operating in tapping mode with an asymmetric Michelson interferometer. By focusing laser light onto the apex of a metallic AFM tip and detecting the back-scattered light at higher harmonics of the tapping frequency, a spatial resolution of around 20 nm, independent of the wavelength and determined by the tip apex size is achieved.[63,64] The system under study can be regarded as a weak scatterer with an optical phase signal that is, in good approximation, proportional to the absorption.[65] IR-SNOM can be operated in both spectroscopy mode and imaging mode. Given that the electric field enhancement in IR-SNOM is aligned with the tip oscillation axis, predominantly vibrational modes with a dipole moment perpendicular to the substrate are excited, resulting in IR-SNOM being sensitive for molecular orientation.[66] A Zn-DMOF was grown with slightly modified conditions to obtain individual crystals, as shown in **Figure 6a**. Spectra were recorded on two individual crystals exhibiting different orientations, one of the platelets was lying flat, while the other one was standing upright. The corresponding spectra, presented in Figure 6b, exhibit strong orientation-dependent signatures. Specifically, the flat platelet displays a strong signal at 1640 cm^{-1} and a weak one at 1407 cm^{-1}, whereas the upright standing platelet displays the opposite behavior, a weak signal at 1640 cm^{-1} and a strong one at 1407 cm^{-1}. This trend is consistent with simulations of the effective permittivity, shown in Figure 3a, that predict a significant orientation dependence. At around 1600 cm^{-1}, simulations indicate a dominant resonance for the zz-component and a negligible response for the xx- and yy-component, respectively. At about 1400 cm^{-1}, the opposite is predicted and experimentally confirmed, strong resonance for the xx- and yy-component and a significantly lower one for the zz-component. Since the spectral differences between the platelet orientations are most pronounced at 1407and 1640 cm^{-1}, these

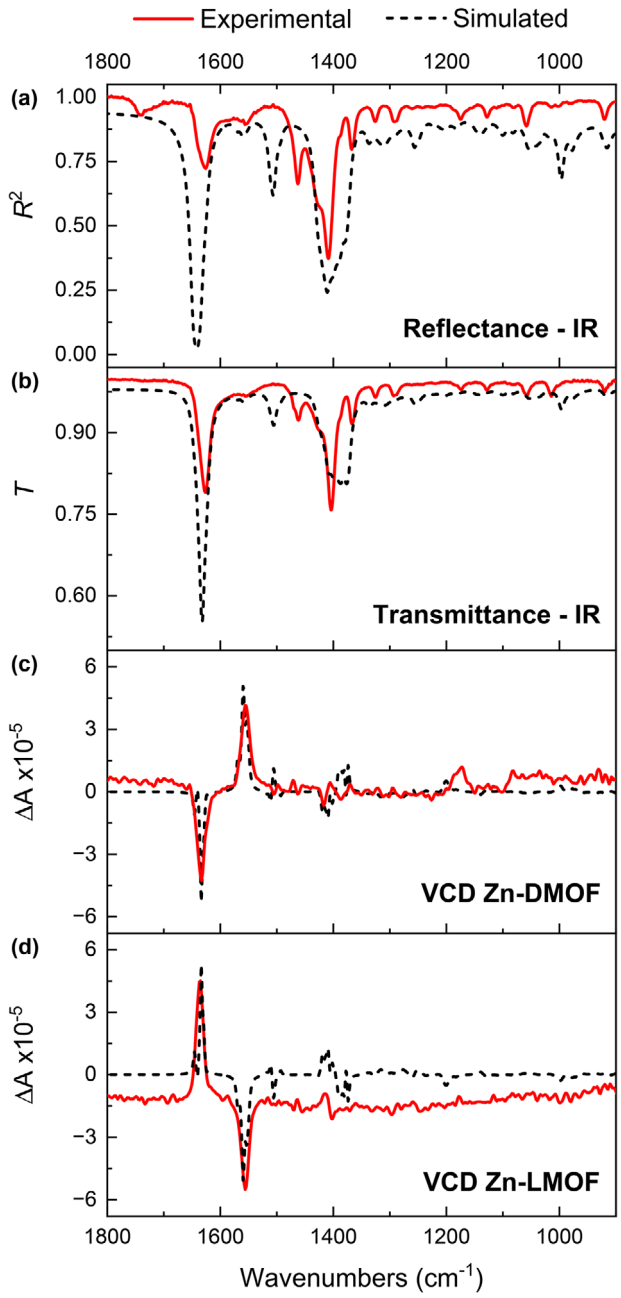

Figure 5. Comparison between Maxwell scattering simulations and experimental measurements of a) Squared power reflectance, b) power transmittance and VCD of c) Zn-DMOF and d) Zn-LMOF.

wavelengths were selected for IR imaging (see Figure 6c,d). The IR-SNOM images reveal that the flat platelets exhibit a high signal intensity at 1640 cm^{-1}, while the upstanding platelet shows a low signal intensity. For excitation at 1407 cm^{-1}, the relative signal intensities of the different crystallite types are vice versa, as was anticipated from the spectra. Due to the relatively large aspect ratio of the upstanding platelet, it was possible to manipulate its orientation with the help of an AFM tip. After manipulation shown in Figure 6e–h, the optical response of the reoriented crystal was observed to match that of an unmanipulated flat platelet, thereby proving that the observed spectral differences result from a difference in molecular orientation.

3. Conclusion

In this work, we presented and validated a multi-scale approach for predicting the optical properties of chiral SURMOFs. The model spans several length scales - from the unit cell to the thin-film level - by linking quantum-chemical calculations with Maxwell-based scattering simulations. Comparison with experimental data from infrared spectroscopy and circular dichroism showed good agreement between simulated and measured spectra. We also demonstrated that SURMOFs are well-suited for solid-state VCD measurements, as the use of a transparent substrate at the desired wavelengths eliminates the need for any additional preparation. The simulated VCD spectra were in very good agreement with the experimental ones, and it confirms how some vibrational modes that were not so active in the IR, were more active in the VCD. Additionally, IR-SNOM measurements revealed orientation-dependent IR absorption in the crystals, helping to explain intensity differences between the simulated and experimental IR bands. This was further confirmed by evaluating the optical response of the same crystal in both orientations. To further improve the already good agreement between theoretical predictions and experimental observations, future developments of our workflow are envisaged, where the finite-size molecular modeling of light-matter interactions could potentially be replaced with full periodic TDDFT calculations. Furthermore, Maxwell scattering simulations could include the Cu-MOF seed layers. However, such improvements require significant efforts in theory development, increase computational cost and energy consumption, and are outside the scope of this publication.

In general, this study highlights the importance of combining experimental results with theoretical modeling in the development of functional SURMOFs. By confirming the usability of such models, we intend to provide a promising pathway for the accelerated discovery and application of chiral MOFs.

4. Experimental Section

Materials: The substrates used for SURMOF deposition were prepared by first coating silicon wafers with a 5 nm adhesion layer of titanium, followed by a 100 nm gold layer. In this work, these substrates were referred to as gold substrates. CaF_2 windows of 1 mm thickness and 20 mm diameter (Korth Kristalle GmbH) and quartz windows of 1 mm thickness and 20 mm diameter (GVB GmbH) were also used as optically transparent substrates. All chemicals were purchased from commercial suppliers and used without further purification: camphoric acid (1,2,2-Trimethyl-1,3-cyclopentanedicarboxylic acid) enantiomers (Thermo Scientific), zinc acetate dihydrate and 1,4-diazabicyclo [2.2.2]octane (DABCO) (Merck), copper (II) acetate monohydrate and ethanol (VWR Chemicals).

Substrate Treatments: All substrates underwent specific treatments for surface activation or functionalization. The gold substrates were functionalized with a self-assembled monolayer (SAM) of 11-Mercapto-1-undecanol (MUD). Before functionalization, the substrates were washed with ethanol, followed by immersion in the MUD solution for 24 h. After this period, they were rinsed again with ethanol to remove unreacted molecules and subsequently dried with N_2. CaF_2 substrates were cleaned with ethanol and subjected to O_2 plasma treatment for 30 min before use. Similarly, the quartz windows were washed with ethanol and treated in a UV/Ozone reactor for 15 min prior to use. To ensure optimal surface

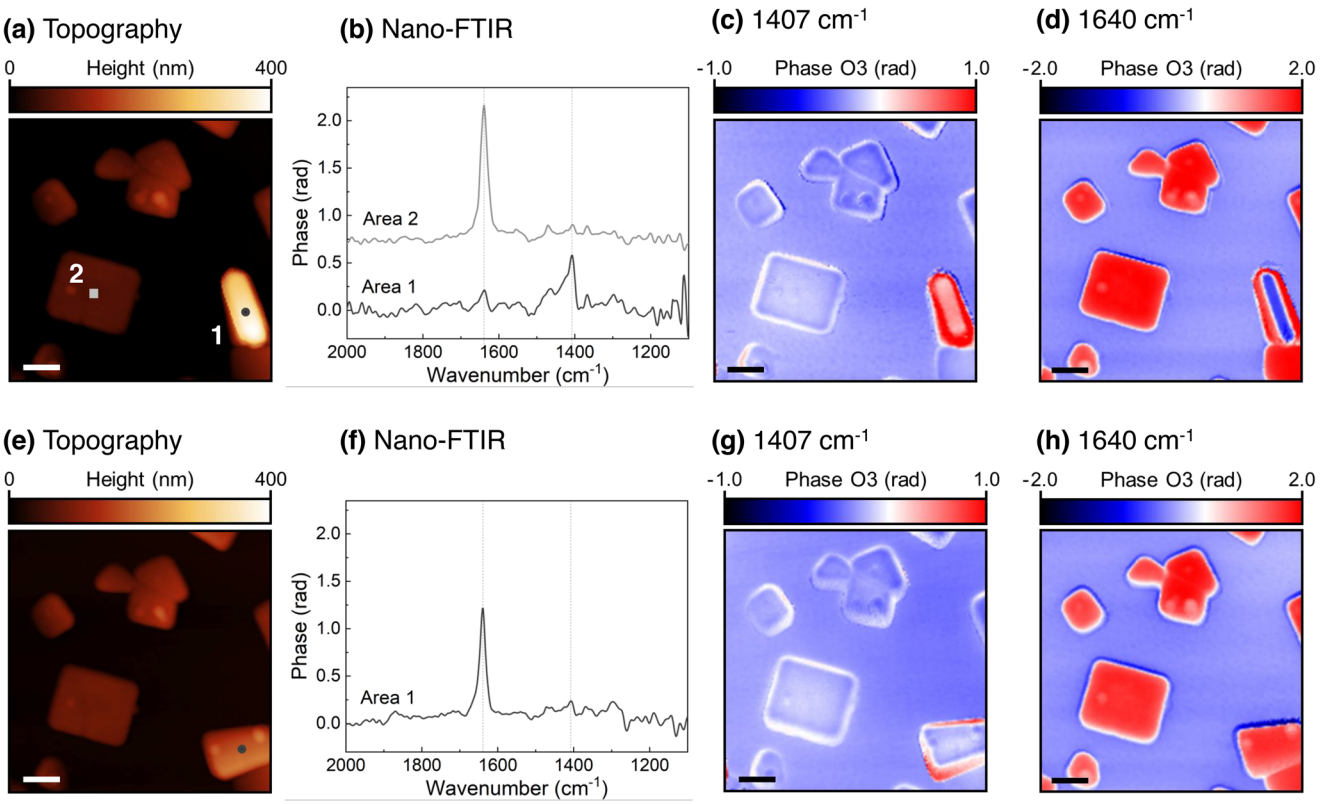

Figure 6. a) AFM height image of the Zn-DMOF. b) Stacked near-field nano-FTIR phase spectra measured at the locations marked in a. The vertical dashed lines correspond to 1407 and 1640 cm^{-1}. IR-SNOM optical phase image recorded at c) 1407 cm^{-1} and d) 1640 cm^{-1}. e–h) Respective data after manipulation of the orientation of the crystal at the bottom right corner with an AFM tip. Scale bars = 500 nm.

adhesion, all substrates were immersed in the metal solution immediately after treatment. The choice of the substrate depended on the specific requirements of each optical characterization technique. IR transmission measurements and VCD were performed using CaF_2 substrates, while gold substrates were used for reflectance measurements and SNOM. ECD measurements were performed on quartz substrates.

SURMOF Growth: From the different methods available for SURMOF fabrication,[67] in this work, the immersion approach realized by a pump-based system was chosen. Substrates were placed inside a double-walled vessel, while a four-channel pump was used to sequentially introduce and remove chemical solutions following the order: Metal > First Rinse > Second Rinse > Linker > First Rinse > Second Rinse. All solutions used in this process were made with ethanol, which was also the solvent used for rinsing. The metal solution was composed of 1 mM copper or zinc acetate, while the linker solution contained both linkers at the following concentrations: 0.2 mM DABCO and 0.2 mM camphoric acid. The residence times for each precursor were 15 min for the metal solution and 25 min for the linker solution.

Each complete sequence of steps constituted a single deposition cycle. The number of cycles was adjusted to control the thickness of the SURMOFs, depending on the specific characterization requirements. The double-walled vessel enabled temperature control by circulating water at 65 °C, ensuring optimal reaction conditions.

Details about the SURMOF characterization could be found in the Supporting Information.

Supporting Information

Supporting Information is available from the Wiley Online Library or from the author.

Acknowledgements

A.F., C.W., N.v.C., M.K., C.H. P.T., and C.R. acknowledged support by the Deutsche Forschungsgemeinschaft (DFG, German Research Foundation) under Germany's Excellence Strategy via the Excellence Cluster 3D Matter Made to Order (EXC-2082/1-390761711). M.K. and C.R. acknowledged funding from the Carl Zeiss Foundation via the CZF-Focus@HEiKA Program. M.K. and C.R. acknowledged funding by the Volkswagen Foundation. C.R. acknowledged support by the Helmholtz Association via the Helmholtz program "Materials Systems Engineering" (MSE). B.Z. and C.R. acknowledged support by the KIT through the "Virtual Materials Design" (VIRTMAT) project. The authors thank Dr. Markus Nyman for the fruitful discussions. M.K. and C.R. acknowledged support by the state of Baden–Württemberg through bwHPC and the German Research Foundation (DFG) through grant no. INST 40/575-1 FUGG (JUSTUS 2 cluster) and the HoreKa supercomputer funded by the Ministry of Science, Research and the Arts Baden–Württemberg and by the Federal Ministry of Education and Research.

Open access funding enabled and organized by Projekt DEAL.

Conflict of Interest

The authors declare no conflict of interest.

Data Availability Statement

The data that support the findings of this study are available in the supplementary material of this article.

Keywords

chiral surface-anchored metal-organic frameworks, infrared scanning near-field optical microscopy, multiscale modeling, solid-state vibrational circular dichroism

Received: September 10, 2025
Revised: October 27, 2025
Published online:

[1] R. Freund, O. Zaremba, G. Arnauts, R. Ameloot, G. Skorupskii, M. Dincă, A. Bavykina, J. Gascon, A. Ejsmont, J. Goscianska, M. Kalmutzki, U. Lächelt, E. Ploetz, C. S. Diercks, S. Wuttke, *Angew. Chem., Int. Ed.* **2021**, *60*, 23975.
[2] W. Gong, Z. Chen, J. Dong, Y. Liu, Y. Cui, *Chem. Rev.* **2022**, *122*, 9078.
[3] H. Li, M. Eddaoudi, M. O'Keeffe, O. M. Yaghi, *Nature* **1999**, *402*, 276.
[4] M. Kondo, T. Yoshitomi, H. Matsuzaka, S. Kitagawa, K. Seki, *Angew. Chem.* **1997**, *36*, 1725.
[5] Y. Luo, S. Bag, O. Zaremba, A. Cierpka, J. Andreo, S. Wuttke, P. Friederich, M. Tsotsalas, *Angew. Chem., Int. Ed.* **2022**, *61*, e202200242.
[6] T. Jia, Y. Gu, F. Li, *J. Environ. Chem. Eng.* **2022**, *10*, 108300.
[7] L. Pilz, C. Natzeck, J. Wohlgemuth, N. Scheuermann, S. Spiegel, S. Oßwald, A. Knebel, S. Bräse, C. Wöll, M. Tsotsalas, N. Prasetya, *J. Mater. Chem. A* **2023**, *11*, 24724.
[8] Q. Qian, P. A. Asinger, M. J. Lee, G. Han, K. M. Rodriguez, S. Lin, F. M. Benedetti, A. X. Wu, W. S. Chi, Z. P. Smith, *Chem. Rev.* **2020**, *120*, 8161.
[9] Y. Zhang, X. Yu, Y. Hou, C. Liu, G. Xie, X. Chen, *Mol. Catal.* **2024**, *555*, 113851.
[10] R. Greifenstein, T. Ballweg, T. Hashem, E. Gottwald, D. Achauer, F. Kirschhöfer, M. Nusser, G. Brenner-Weiß, E. Sedghamiz, W. Wenzel, E. Mittmann, K. S. Rabe, C. M. Niemeyer, M. Franzreb, C. Wöll, *Angew. Chem., Int. Ed.* **2022**, *61*, e202117144.
[11] I. A. Lázaro, X. Chen, M. Ding, A. Eskandari, D. Fairen-Jimenez, M. Giménez-Marqués, R. Gref, W. Lin, T. Luo, R. S. Forgan, *Nat. Rev. Methods Primers* **2024**, *4*, 42.
[12] N. Kajal, V. Singh, R. Gupta, S. Gautam, *Environ. Res.* **2022**, *204*, 112320.
[13] H. Yuan, N. Li, W. Fan, H. Cai, D. Zhao, *Adv. Sci.* **2022**, *9*, 2104374.
[14] N. Stock, S. Biswas, *Chem. Rev.* **2012**, *112*, 933.
[15] O. Shekhah, H. Wang, S. Kowarik, F. Schreiber, M. Paulus, M. Tolan, C. Sternemann, F. Evers, D. Zacher, R. A. Fischer, C. Wöll, *J. Am. Chem. Soc.* **2007**, *129*, 15118.
[16] L. Heinke, C. Wöll, *Adv. Mater.* **2019**, *31*, 1806324.
[17] D.-H. Chen, H. Gliemann, C. Wöll, *Chem. Phy. Rev.* **2023**, *4*, 011305.
[18] R. Haldar, L. Heinke, C. Wöll, *Adv. Mater.* **2020**, *32*, 1905227.
[19] Y.-H. Xiao, Y.-B. Tian, Z.-G. Gu, J. Zhang, *EnergyChem* **2021**, *3*, 100065.
[20] J. Liu, C. Wöll, *Chem. Soc. Rev.* **2017**, *46*, 5730.
[21] Q. Ye, J. Li, Y. Huang, H. Wu, Y. Li, B. Yan, *J. Environ. Chem. Eng.* **2023**, *11*, 109250.
[22] Z.-G. Gu, J. Bürck, A. Bihlmeier, J. Liu, O. Shekhah, P. G. Weidler, C. Azucena, Z. Wang, S. Heissler, H. Gliemann, W. Klopper, A. S. Ulrich, C. Wöll, *Chem. - Eur. J.* **2014**, *20*, 9879.
[23] M. Krupová, V. Andrushchenko, *Spectrochim. Acta Part A: Mol. Biomol. Spectr.* **2025**, *340*, 125839.
[24] S. Jähnigen, *Angew. Chem., Int. Ed.* **2023**, *62*, e202303595.
[25] S. Zhang, D. Li, D. Guo, H. Zhang, W. Shi, P. Cheng, L. Wojtas, M. J. Zaworotko, *J. Am. Chem. Soc.* **2015**, *137*, 15406.
[26] D. Földes, E. Kováts, G. Bortel, K. Kamarás, G. Tarczay, E. Jakab, S. Pekker, *J. Mol. Struct.* **2022**, *1257*, 132538.
[27] L. D. B. Mandemaker, M. Rivera-Torrente, R. Geitner, C. M. Vis, B. M. Weckhuysen, *Angew. Chem., Int. Ed.* **2020**, *59*, 19545.
[28] S. Srivastava, S. P. Shet, S. S. Priya, K. Sudhakar, M. Tahir, *Int. J. Hydrogen Energy* **2022**, *47*, 15820.
[29] Y. Guo, S. Zhang, M. Pu, Q. He, J. Jin, M. Xu, Y. Zhang, P. Gao, X. Luo, *Light: Sci. Appl.* **2021**, *10*, 63.
[30] J. Chen, F. Yu, X. Liu, Y. Bao, R. Chen, Z. Zhao, J. Wang, X. Wang, W. Liu, Y. Shi, C.-W. Qiu, X. Chen, W. Lu, G. Li, *Light: Sci. Appl.* **2023**, *12*, 105.
[31] J. Li, X. Lu, H. Li, C. Song, Q. Tan, Y. He, J. Liu, L. Luo, T. Tang, T. Liu, H. Xu, S. Xiao, W. Huang, Y. Shen, Y. Zhang, Y. Zhang, J. Yao, *Opto-Electron. Adv.* **2024**, *7*, 240075.
[32] H. Hurwitz, R. C. Jones, *J. Opt. Soc. Am.* **1941**, *31*, 493.
[33] P. Waterman, *Proc. IEEE* **1965**, *53*, 805.
[34] B. Zerulla, C. Li, D. Beutel, S. Oßwald, C. Holzer, J. Bürck, S. Bräse, C. Wöll, I. Fernandez-Corbaton, L. Heinke, C. Rockstuhl, M. Krstić, *Adv. Funct. Mater.* **2024**, *34*, 2301093.
[35] M. Bieri, C. Gautier, T. Bürgi, *Phys. Chem. Chem. Phys.* **2007**, *9*, 671.
[36] C. R. Lightner, F. Desmet, D. Gisler, S. A. Meyer, A. F. Perez Mellor, H. Niese, A. Rosspeintner, R. C. Keitel, T. Bürgi, W. A. Herrebout, C. Johannessen, D. J. Norris, *ACS Photonics* **2023**, *10*, 475.
[37] F. Bertorelle, I. Russier-Antoine, N. Calin, C. Comby-Zerbino, A. Bensalah-Ledoux, S. Guy, P. Dugourd, P.-F. Brevet, Ž. Sanader, M. Krstić, V. Bonačić-Koutecký, R. Antoine, *J. Phys. Chem. Lett.* **2017**, *8*, 1979.
[38] S. Basu, M. Perić Bakulić, Ž. Sanader Maršić, V. Bonačić-Koutecký, N. Amdursky, *ACS Nano* **2023**, *17*, 16644.
[39] E. Mohammadi, G. Tagliabue, *ACS Photonics* **2025**, *12*, 152.
[40] A. Amirjani, T. V. Tsoulos, S. H. Sajjadi, A. Antonucci, S.-J. Wu, G. Tagliabue, D. F. Haghshenas, A. A. Boghossian, *Carbon* **2022**, *194*, 162.
[41] Z. Haddadin, A. M. Nguyen, L. V. Poulikakos, *Light: Sci. Appl.* **2024**, *13*, 45.
[42] Z. Haddadin, A. M. Nguyen, L. V. Poulikakos, *Opt. Express* **2025**, *33*, 11731.
[43] Z. Xu, Y. Liu, A. Chandresh, P. B. Pati, V. Monnier, L. Heinke, F. Odobel, S. Diring, R. Haldar, C. Wöll, *Adv. Funct. Mater.* **2024**, *34*, 2308847.
[44] F. ZareKarizi, M. Joharian, A. Morsali, *J. Mater. Chem. A* **2018**, *6*, 19288.
[45] D. N. Dybtsev, M. P. Yutkin, E. V. Peresypkina, A. V. Virovets, C. Serre, G. Férey, V. P. Fedin, *Inorg. Chem.* **2007**, *46*, 6843.
[46] Z.-G. Gu, C. Zhan, J. Zhang, X. Bu, *Chem. Soc. Rev.* **2016**, *45*, 3122.
[47] Y. Zhu, T. Ding, X. Zhang, Y. Zhou, J. Yu, X. Li, H. Zheng, Z. Sun, C. Jiao, *Inorg. Chem. Front.* **2023**, *10*, 2818.
[48] A. Hubber, C. Hua, *Chem. - Eur. J.* **2024**, *30*, e202400071.
[49] B. Liu, O. Shekhah, H. K. Arslan, J. Liu, R. A. Fischer, C. Wöll, *Angew. Chem.* **2011**, *51*, 807.
[50] Z. Sharifzadeh, K. Berijani, A. Morsali, *Coord. Chem. Rev.* **2021**, *445*, 214083.
[51] Y. Zhu, Y. Zhou, X. Zhang, Z. Sun, C. Jiao, *Adv. Opt. Mater.* **2021**, *9*, 2001889.
[52] L. A. Hall, D. M. D'Alessandro, G. Lakhwani, *Chem. Soc. Rev.* **2023**, *52*, 3567.
[53] A. Gheorghe, B. Strudwick, D. M. Dawson, S. E. Ashbrook, S. Woutersen, D. Dubbeldam, S. Tanase, *Chem. - Eur. J.* **2020**, *26*, 13957.
[54] R. Haldar, C. Wöll, *Nano Res.* **2021**, *14*, 355.
[55] B. Zerulla, M. Krstić, D. Beutel, C. Holzer, C. Wöll, C. Rockstuhl, I. Fernandez-Corbaton, *Adv. Mater.* **2022**, *34*, 2200350.
[56] T. D. Kühne, M. Iannuzzi, M. Del Ben, V. V. Rybkin, P. Seewald, F. Stein, T. Laino, R. Z. Khaliullin, O. Schütt, F. Schiffmann, D. Golze, J. Wilhelm, S. Chulkov, M. H. Bani-Hashemian, V. Weber, U. Borštnik, M. Taillefumier, A. S. Jakobovits, A. Lazzaro, H. Pabst, T. Müller, R. Schade, M. Guidon, S. Andermatt, N. Holmberg, G. K. Schenter, A. Hehn, A. Bussy, F. Belleflamme, G. Tabacchi, et al., *J. Chem. Phys.* **2020**, *152*, 194103.

[57] TURBOMOLE 7.7 2022, a development of University of Karlsruhe and Forschungszentrum Karlsruhe GmbH, TURBOMOLE GmbH, **2007**, https://www.turbomole.org.
[58] Y. J. Franzke, C. Holzer, J. H. Andersen, T. Begušić, F. Bruder, S. Coriani, F. Della Sala, E. Fabiano, D. A. Fedotov, S. Fürst, S. Gillhuber, R. Grotjahn, M. Kaupp, M. Kehry, M. Krstić, F. Mack, S. Majumdar, B. D. Nguyen, S. M. Parker, F. Pauly, A. Pausch, E. Perlt, G. S. Phun, A. Rajabi, D. Rappoport, B. Samal, T. Schrader, M. Sharma, E. Tapavicza, R. S. Treß, et al., *J. Chem. Theory Comput.* **2023**, *19*, 6859.
[59] Z.-G. Gu, S. Grosjean, S. Bräse, C. Wöll, L. Heinke, *Chem. Commun.* **2015**, *51*, 8998.
[60] B. Zerulla, R. Venkitakrishnan, D. Beutel, M. Krstić, C. Holzer, C. Rockstuhl, I. Fernandez-Corbaton, *Adv. Opt. Mater.* **2023**, *11*, 2201564.
[61] T. G. Mayerhöfer, *Wave Optics in Infrared Spectroscopy*, Elsevier Science, Amsterdam **2024**.
[62] W. Theiss, Scout – Software Package for Optical Spectroscopy (v4.29), WTheiss Hardware and Software, 11875 E Elin Ranch Road, Tucson, AZ 85749, USA **2024**.
[63] N. Ocelic, A. Huber, R. Hillenbrand, *Appl. Phys. Lett.* **2006**, *89*, 101124.
[64] A. Centrone, *Annu. Rev. Anal. Chem.* **2015**, *8*, 101.
[65] F. Huth, A. Govyadinov, S. Amarie, W. Nuansing, F. Keilmann, R. Hillenbrand, *Nano Lett.* **2012**, *12*, 3973.
[66] V. J. Rao, M. Matthiesen, K. P. Goetz, C. Huck, C. Yim, R. Siris, J. Han, S. Hahn, U. H. F. Bunz, A. Dreuw, G. S. Duesberg, A. Pucci, J. Zaumseil, *J. Phys. Chem. C* **2020**, *124*, 5331.
[67] Z. Wang, C. Wöll, *Adv. Mater. Technol.* **2019**, *4*, 1800413.